Kinematics-based Tracking Control Method for Operational Robotic Arm Under Multi-Environmental Constraints

Li Zhou[1] ✉ – Yan Liu[2]

1 School of Mechanical and Electrical Engineering, Hunan City University, China

2 College of Information and Electronic Engineering, Hunan City University, China

✉ 13617375587@163.com

Abstract *The environmental hazards associated with coal mining operations are extremely high, making the use of robotic arms to replace manual labor crucial for improving both the safety and cost-effectiveness of the work process. To address the various environmental constraints, such as spatial limitations, obstacles, and internal and external disturbances, this study proposes a kinematic-based tracking and control method for mining robotic arm. The objective of this numerical study is to mitigate the impact of environmental constraints on the stability of robotic arms, ensuring that they can maintain high precision and stability in complex operating conditions. Simulation results showed that the proposed method enabled the robotic arm to achieve operational thrust peaks exceeding 13,968 N and screw torque peaks greater than 0.06 Nm. The system reached steady state in an average of 0.24 s, with an error reduction of 2.3 %. Compared to other methods, the disturbance tracker reduced the average error by 2 %, and the feedback controller decreased the prediction lag by 5 %. Overall, this method significantly enhances the accuracy and stability of robotic arms in coal mining operations, making it a promising approach for real-world applications.*

Keywords *coal mining operations, robotic arm, dynamics, multi-environmental constraints, tracking control*

Highlights

- *The control method for mining robot arm movement explicitly accounts for environmental constraints.*
- *Fifth-degree interpolation is applied to smooth motion control, enhance performance, and improve energy efficiency.*
- *A hybrid control strategy combines proportional-integral-derivative (PID) control with adaptive control to reduce errors and increase robustness.*

1 INTRODUCTION

Currently, most coal mines still rely on traditional manual operation methods. The high complexity and harsh conditions of coal mining environments expose miners to significant risks for prolonged periods. Moreover, work accuracy is often affected by environmental factors [1]. With the growing demand for improved safety and accuracy in coal mining and the advancement of automation and intelligent machinery, the prospect of unmanned coal mining is becoming increasingly feasible [2]. The key enabler of unmanned mining is the application of multi-joint robot arm (RA), which can perform the coal extraction tasks through coordinated joint rotation and displacement [3]. However, numerous internal and external disturbances limit the development of RA anthropomorphism. Therefore, achieving more accurate modeling parameters and effective tracking control remains a central challenge in the RA research [4]. Minimizing RA trajectory tracking errors through a combination of control schemes and anti-interference techniques is critical for advancing unmanned mining technology [5].

Many experts and scholars have conducted extensive research on control strategy for the dynamic modeling of RA, providing a solid foundation for subsequent trajectory planning. Lattanzi et al. [6] proposed a sliding-mode-based RA control technique aimed at addressing motion synchronization control issues. Their outcomes demonstrated that the approach could successfully develop a simulation model that satisfies the automation criteria of heavy-duty RAs. To quantify system perturbations, Li et al. [7] presented a neural network-based control technique. The outcomes revealed that this approach could accurately predict the degree environmental uncertainties affect RA, resulting precise location monitoring. Zahaf et al. [8] proposed an adaptive slip film-based control method that solved the disturbance prediction problems in hydraulic systems. Simulation tests quantified and compensated for external disturbances effectively [8]. Jouila et al. [9] proposed a control strategy based on calculus combinations that addresses the saturation problem of disturbance quantities during model construction. This method effectively improved the control strategy upon traditional control strategies, simplifying the simulation model construction process while enhancing effectiveness [9]. Cheng et al. [10] proposed a bias-correction-based control strategy, capable of learning from large amount of historical data to correct the bias in ongoing prediction task. The findings indicated that this technique successfully increased the RA's operational flexibility and response time while reducing excessive vibration [10].

Numerous researchers have also focused on enhancing the RA anti-interference tracking capabilities. Lei et al. [11] proposed a particle-swarm-based RA parameter algorithm optimization technique to increase the precision of joint position and velocity prediction accuracy. The findings illustrated that this method effectively addressed the effects of angular friction, self-weight, and inertia on trajectory deviation, thereby improving the tracking accuracy [11]. Liu et al. [12] developed a kinetic model based on moment calculations to quantify the influence of Coriolis and centrifugal forces on RA motion. The strategy was found to be effective in realizing moment compensation, ensuring regular control, and preventing tracking deviation. Liu et al. [13] proposed a distributed neural adaptive fault-tolerant control method for multi-flexible RAs under combined interference from actuator failures, input saturation, and external disturbances. By employing a second-order auxiliary system to eliminate input saturation effect and reconstructing boundary dynamics as a second-order system using proportional-integral auxiliary variables", the results successfully achieved cooperative fault-tolerant control in networked flexible RA systems. Liu et al. [14] proposed a hybrid control strategy using an infinite-dimensional disturbance observer for the vibration suppression and attitude tracking control of flexible RAs under external disturbances. The research established a mixed dynamic model that coupled partial and ordinary differential equations. Two types of control laws were designed to suppress vibration: boundary and distributed. The results verified global asymptotic stability and effectiveness in vibration suppression. In another work Liu et al. [15] proposed a boundary control strategy based on perturbation observers to address the vibration suppression issue in axially moving RAs with input constraints. Their research aimed to minimize the vibration offset of the RA's flexible components by designing boundary control laws and introducing auxiliary terms to address the actuator input saturation limit. Experimental validation confirmed the proposed approach's capability to achieve high-precision control of complex flexible mechanical systems in challenging conditions.

In summary, many methods have been proposed to address RA environmental constraints and tracking control strategies, contributing to the advancement of intelligent robotics. However, existing research still face limitations in maintaining high tracking control performance under compound disturbances and continuous operation requirements. In many cases, control accuracy and stability remain insufficient for the existing operational demands. To address these challenges, this study proposes a kinematic-based tracking control method for RA under multiple environmental constraints. It aims to enhance stability and control accuracy of the RA under multiple environmental constraints and composite interference conditions. The key innovation lies in the development of an RA dynamic simulation model capable of adapting to diverse environmental constraints while mitigating the effect of multiple disturbing factors. Moreover, the integration of multiple controllers reduces tracking errors and ensures the continuity and reliability of RA joint motion in multiple operation processes. The primary research contribution lies in the construction of perturbation trackers and error feedback controllers (EFCs), which effectively minimize tracking errors, ensure the continuity and reliability of the robotic arm's joint motion, and improve the adaptability under complex disturbance conditions. Compared to existing control schemes, the proposed method greatly improves RA's operational stability and tracking control performance in complex environments. It does so by enhancing prediction accuracy, reducing error, and minimizing control lag.

2 METHODS

In this section, the improved Denavit-Hartenberg (D-H) parametric method is first applied to construct the RA linkage coordinate system (CS), with its feasibility verified using both forward and inverse kinematics. The RA workspace is further derived to optimize its structural parameters. Subsequently, joint velocities and spatial mapping are performed using Jacobian matrix. Finally, trajectory planning is implemented using the fifth-degree interpolation method. To mitigate errors caused by various disturbing factors, an anti-disturbance tracker is employed in combination with adaptive tuning and a proportional-integral-derivative (PID) control strategy.

2.1 Modeling of Operational RA Kinematics Based on Multi-Environmental Constraints

At present, coal mining environments are still harsh and complex, which makes RAs susceptible to interference from internal and environmental factors. Therefore, the operational RA performance requirements have become increasingly stringent to ensure efficiency and safety in coal mining processes [16]. To construct a simulation model of an RA under multi-environmental constraints, it is essential to consider its full operational sequence. The main operation process begins with extending the RA to reach the target position, followed by fine-tuning the position using an adaptive control (AC) tracker. A camera is then used to detect the roadway conditions. Once the target hole is reached, the RA is used for ore excavation and handling [17]. The study begins with the structural design of the RA to satisfy the coupling with multi-environmental constraints [18]. Based on the improved D-H parameters (DHPs), the RA linkage CS is established on the three RA models, with the coordinate axes directions specified, as shown in Fig. 1 [19].

According to the RA linkage CS established in Fig. 1, the angular and linear parameters for each joint of RA are determined. Since the RA consists of multiple connecting rods and joints, a right-angle CS is established for each joint. Therefore, the positions and orientations of connecting rods and joints can be expressed using homogeneous transformation matrix to obtain the RA end position and orientation as shown in Eq. (1).

$$ {}^{i-1}_{i}T = \begin{bmatrix} \cos\theta_i & -\sin\theta_i\cos\alpha_i & \sin\theta_i\sin\alpha_i & a_i\cos\theta_i \\ \sin\theta_i & \cos\theta_i\cos\alpha_i & -\cos\theta_i\sin\alpha_i & a_i\sin\theta_i \\ 0 & \sin\alpha_i & \cos\alpha_i & d_i \\ 0 & 0 & 0 & 1 \end{bmatrix}. \tag{1} $$

Here, ${}^{i-1}_{i}T$ is the expression of the degree of association between two connecting rod coordinates i and $i-1$. θ_i is the angle of rotation of the Z_i rod around the X_i rod connected to the same joint. α_i is the angle of rotation of the X_i rod around the Z_i rod attached to the same

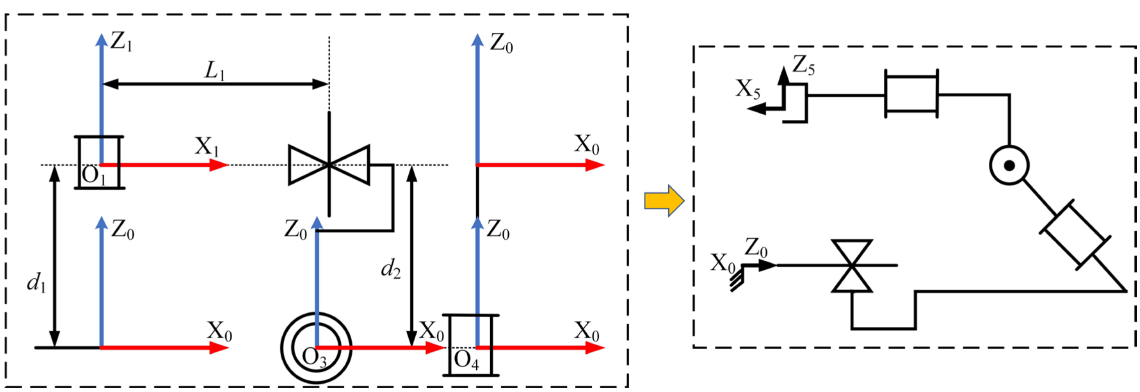

Fig. 1. Structural diagram of the coordinate system of the RA

joint. d_i denotes the displacement length along the X_i axis in the joint CSi. The established RACS and the final orientation are verified by positive kinematics. The positional-orientation correlation matrix of the RA can be obtained by substituting the joint angle (JA) parameters obtained from the CS established by improving the DHP into the transformation matrix and multiplying them as shown in Eq. (2).

$$\begin{bmatrix} {}^0R & {}^0P \\ 0 & 1 \end{bmatrix} = \begin{bmatrix} n_x & o_x & a_x & p_x \\ n_y & o_y & a_y & p_y \\ n_z & o_z & a_z & p_z \\ 0 & 0 & 0 & 1 \end{bmatrix}. \tag{2}$$

Here, n represents the unit direction vector of the X-axis of the end effector CS, o represents the unit direction vector representing the Y-axis of the end effector CS, a represents the unit direction vector representing the Z-axis of the end effector CS, p represents the origin position of the end effector CS, ${}^0R$ represents the final posture obtained by the robotic arm, and ${}^0P$ represents the final position obtained by the robotic arm. JA is a known parameter because the RA rotation angle has been obtained through the linkage CS at the beginning. The final position of the RA can be obtained by substituting the known JAs into its sub-transformation matrix. Thus, the positive kinematic analysis (KA) of the RA model can be verified. The following inverse KA of the RA is carried out. The six-degree-of-freedom joint rotation simulation model of the RA is constructed by applying MATLAB/Simulink R2022a, as shown in Fig. 2.

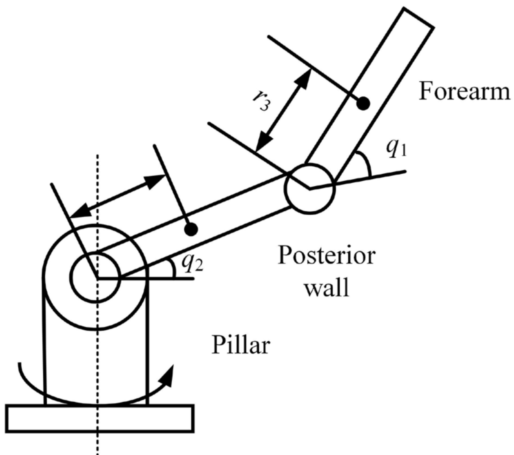

Fig. 2. Schematic diagram of a RA with two rotational joints

After the robot joints are built in MATLAB using DHP, the *Link* function is used to generate the associated connecting rods around the joints. Then the *Serial* class function is used to connect the joints and their corresponding connecting rods to form a complete robotic arm simulation model (RASM). The joint rotation angle (JRA) of the RASM is assumed to be 0°. Then the final position and orientation of the RA are obtained by solving its sub-transformation matrix using the kinetic *fkine* function, as shown in Eq. (3).

$$T = \begin{bmatrix} 1.000 & 0 & 0 & 0.196 \\ 0 & -1.000 & 0 & 0.038 \\ 0 & 0 & -1.000 & 0.052 \\ 0 & 0 & 0 & 1.000 \end{bmatrix}. \tag{3}$$

Here, T is the final position and orientation of the RA obtained by inverse KA. The simulation model's accuracy is evaluated by comparing its results with the final data obtained from the homogeneous transformation matrix corresponding to the inverse KA process, as described in reference [20]. To ensure the precise RA's handling and grasping of targets during the mining operation, additional control over its characteristics must be applied throughout its movement.

The RA simulation dynamics model is developed in MATLAB with the initial position defined as the starting point. Equation (4) illustrates the application of the fifth-degree polynomial interpolation approach to normalize the parameters associated with the motion velocity, acceleration, and final position of the RA.

$$\theta(t) = A_0 + A_1 t + A_2 t^2 + A_3 t^3 + A_4 t^4 + A_3 t^5. \tag{4}$$

Here, $\theta(t)$ denotes the JRA of the RA at time t. A_0 to A_5 denote the CSs of the corresponding link numbers, respectively. The structural parameters defined during robot planning are then used to generate the RA workspace. The rationality and correctness of the post-configuration structure are verified, and the details of the structure are further optimized. Following joint velocity calculation and spatial mapping via Jacobian matrix, the differential motion position of RA is obtained. Motion process optimization is then carried out as shown in Eq. (5).

$$F(x) = \alpha f_1(x) + \beta f_2(x). \tag{5}$$

Here, α and β denote the weighting coefficients. $F(x)$ represents the objective function to be optimized, while $f_1(x)$ refers to the matrix condition number, and $f_2(x)$ refers the blind zone of RA in the range of operating space. Given that the RA joint motion parameters are known, the joint moments are derived as shown in Eq. (6).

$$\tau = G(q) + V(q, \dot{q}) + M(q)\ddot{q}. \tag{6}$$

Here, τ denotes the joint moment, $M(q)$ represents the inertia matrix, and q. $\dot{q}$ and $\ddot{q}$ correspond to the joint gravity, inertia and centripetal force, respectively. $G(q)$ is the gravity vector, while $V(q, \dot{q})$ is the velocity of motion. This study explores decoupling calculations for joint torques using inverse dynamic analysis of the Jacobian matrix to address the dynamic coupling effect among multiple joints. In particular, the joint torque model is used to separate the inertia matrix, Coriolis force, and centrifugal force term. A feedforward compensation strategy is than implemented to compensate for the coupling torque of each joint in real time. Additionally, when used with the adaptive controller's online parameter adjustment function, this approach corrects nonlinear interference caused by joint coupling in real time. This reduces the influence of one joint on another.

2.2 Anti-Jamming-Based Trajectory Planning Strategy for Operational RA

The above study constructs a RASM that satisfies the forward and inverse dynamics. To further increase the usability of RA-based mining operations, the constructed RASM is next employed for motion trajectory planning and tracking control, as outlined in Fig. 3.

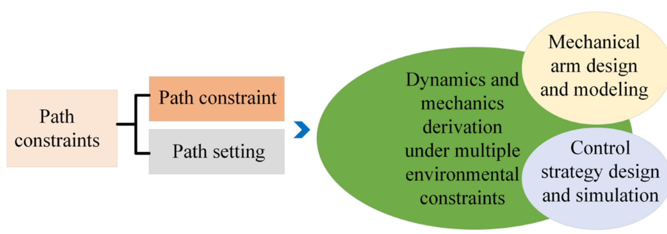

Fig. 3. Trajectory planning process diagram

Since the RA is mainly used to replace manual labor in hazardous production environments, it must operate reliably under dangerous and uncontrollable conditions [21]. Further adjustment and control of model parameters and motion states are required to enable robots to operate efficiently under such complex working conditions while maintaining accuracy and flexibility comparable to that of human operators [22].

As illustrated in Fig. 3, the trajectory control process of the robotic arm is complex and intricate undertaking involving several key stages. These include the construction of the robotic arm simulation model, defining path constraints and settings, performing trajectory planning, implementing trajectory tracking and control, adjusting and optimizing parameters, and other critical tasks. By following the aforementioned steps, the robotic arm can achieve precise and efficient operation even under complex working conditions. Given the complexity of the operating environment, the process begins with planning an anti-interference route for the robot. Subsequently, an anti-disturbance tracker is designed to account for environmental noise amplification, thereby increasing the flexibility of the robot to the environmental conditions. This is shown in Eq. (7).

$$\begin{cases} \dot{\zeta}_1(t) = \zeta_2(t) \\ \dot{\zeta}_2(t) = -\gamma^2(\zeta_1(t) - v_k(t)) - 2\gamma\zeta_2(t) \end{cases}. \tag{7}$$

Here, $\dot{\zeta}_1(t)$ and $\zeta_2(t)$ denote the predicted speed and acceleration of the RA, respectively, $v_k(t)$ is the actual tracking speed, and γ refers to the influencing factors affecting tracking performance. To increase RA stability, a composite observer is used to predict and compensate for its interference, as shown in Eq. (8).

$$\begin{cases} \dot{\xi}(t) = -L^*(\xi(t) + p(x)) \\ \hat{d}_1(t) = \xi(t) + p(x) \end{cases}. \tag{8}$$

Here, $\hat{d}_1(t)$ and L^* are the predicted and actual values of environmental disturbances, respectively, $p(x)$ denotes the non-linear relationship among environmental factors, and $\dot{\xi}(t)$ denotes the observed intermediate variable. The disturbance prediction gain of the composite observer is shown in Eq. (9).

$$L = \frac{\partial p(x)}{\partial x}. \tag{9}$$

The anti-disturbance tracker is used to cope with the prediction and control environmental uncontrollable factors, incorporating adaptive tuning to address the drawback of feed-forward and robustness compensation. Adaptive tuning for controlling nonlinear factors in the RA has proven effective in the absence of time-varying external disturbances. However, in practical application scenarios, numerous operational errors and external state disturbances interfere with the control process, necessitating robust engineering [23,24]. The error values are output with an anti-disturbance tracker, as shown in Eq. (10).

$$e_1(t) = x_1(t) - z_1(t). \tag{10}$$

Here, $e_1(t)$ denotes the error value of the speed estimate, $x_1(t)$ represent the nonlinear relationship of the observed disturbances, and $z_1(t)$ is the actual disturbance factor output. To enhance robustness among independent joints, the entire RA operation process is controlled using the PID strategy following the motion-state decomposition of each joint. Then, the focus of control shifts to the telescopic joints. There, a backstepping adaptive method is applied to identify and adjust the parameters associated with the uncertainty factors of joint motion. The principle of PID control strategy is shown in Fig. 4.

As illustrated in Fig. 4, the PID control system primarily regulates the actual motion state of the telescopic joint by modulating the driving torque of the motor, thereby facilitating accurate tracking of the robotic arm. In particular, the PID controller consists of multiple PID control modules. Each module receives position and velocity error signals and calculates the corresponding control input to adjust the driving torque. This controls joint velocity and position. The backstepping AC approach is a recursive design method for uncertain control systems. It is based on the RA state feedback mechanism and addresses controller stability issues [25,26]. The principle of the method is shown in Fig. 5. The method begins by converting the complex motion states into simple sub-states using the RA state equation. The intermediate sub-states are then controlled using a virtual control law derived from the Lyapunov function. After updating the error-controlled sub-states, the entire motion state is controlled by recursive behavior, enabling the formulation of a complete control law for the overall system.

Inverse step adaptation effectively overcomes the functional control limitations of the controller. Noise measurements are performed across all sub-states of the RA, and all identified noise components of uncertainty are integrated into the external disturbance moment [27,28]. As a result, the RA dynamics equation is formulated in Eq. (11).

$$J\ddot{\theta}_L = \frac{1}{n}T_m - B\dot{\theta}_L + T_{dis}. \tag{11}$$

Here, $\ddot{\theta}_L$ and $\dot{\theta}_L$ denote the angular displacement and velocity of the RA load axis, respectively, J represents the gravity vector, T_m represents the input moment, B represents the time-varying component, T_{dis} represents the output moment, and n represents the joint variable. Parameter adjustment is performed using a hierarchical optimization strategy. The PID gains are initialized based on the frequency domain response [29], the adaptive rate matrix weights are optimized using the particle swarm optimization (PSO) algorithm, and the robust interval of the perturbation observation gain is verified using Monte Carlo sampling [30]. For AC addressing parameter

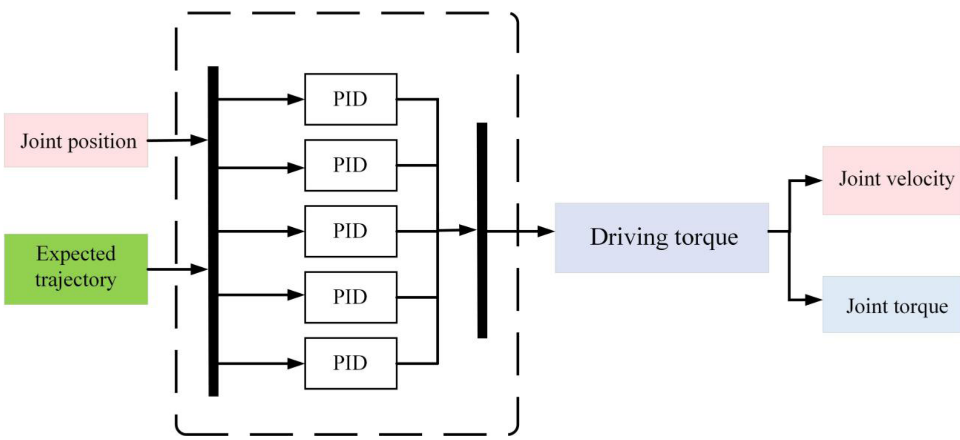

Fig. 4. Schematic diagram of PID control strategy

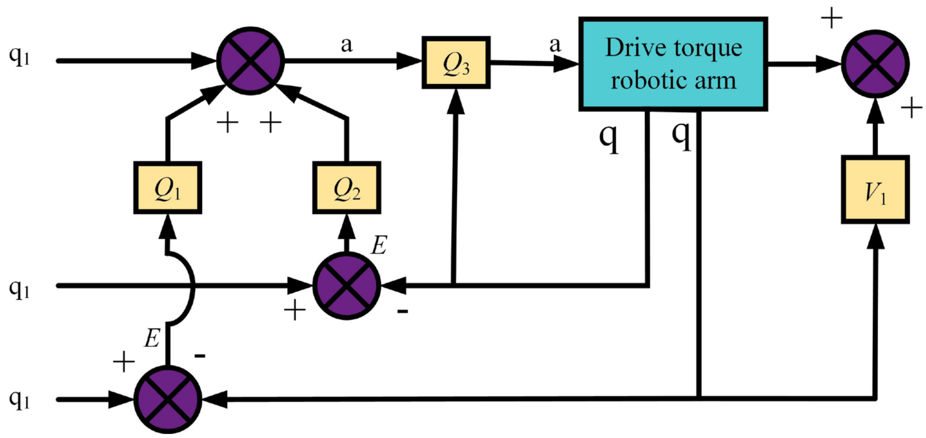

Fig. 5. Schematic diagram of back-stepping adaptive control

uncertainties in the controller, the first step is to define the final angle, as shown in Eq. (12).

$$\theta \in \Omega_\theta \triangleq \{\theta : \theta_{\min} \le \theta \le \theta_{\max}\}. \tag{12}$$

Here, Ω_θ denotes the set of robotic arm joint rotation angles (RAJRAs). θ denotes the current RAJRA. $\theta_{\min}$ is the force matrix of the minimum rotation angle within 1, 2, and 3 minutes. $\theta_{\max}$ is the force matrix for the maximum rotation angle over the same time intervals. The second step involves the Lyapunov function error expressed in Eq. (13).

$$V_2 = V_1 + \frac{1}{2}\theta_1 p^2 + \frac{1}{2}\tilde{\theta}^T \Gamma^{-1} \tilde{\theta}. \tag{13}$$

Here, V_1 and V_2 denote the angular velocity before and after control, respectively, θ_1 represents the current true JRA, $\tilde{\theta}$ is the error between the true angle and the predicted angle, and $\tilde{\theta}^T$ is the transpose of the JRA error. To ensure the stability of the Lyapunov-based control method, the quadratic function of the system state error is selected as the Lyapunov candidate function. This function includes a weighted sum of the squared of the JA error, angular velocity error, and parameter estimation error. By taking the derivative of the Lyapunov function along the closed-loop system trajectory and substituting the adaptive and backstep control laws, it is proven that the derivative consists of a negative-definite component from the error term and the bounded term from parameter estimation error. According to Barbalat's lemma, the joint angular error and the angular velocity error asymptotically converge to zero. This ensures that the negative semi-definite property of the Lyapunov function derivative is preserved under parameter uncertainty, thereby ensuring global asymptotic stability of the closed-loop system. Γ^{-1} denotes the inverse of the adaptive matrix of the controller parameters. The adaptive law governing the parameter matrix is shown in Eq. (14).

$$\dot{\hat{\theta}} = \Gamma \varphi p. \tag{14}$$

Here, $\dot{\hat{\theta}}$ denotes the adaptive law, Γ is the adaptive matrix of controller parameters, φ represents the error value between two adjacent sub-states, and p is the error value between two sub-states of RA. To cope with the constraints of the complex environment, the anti-interference tracker dynamically adjusts the trajectory interpolation parameters by monitoring the relative distance between the end of the robotic arm and the obstacles in real time. When path conflicts are detected, the adaptive controller triggers online parameter correction, re-plans the local path and constrains the joint acceleration to ensure the smooth movement of the robotic arm within a limited space. Meanwhile, the PID controller suppresses the nonlinear disturbances caused by sudden changes in constraints through error feedback, maintaining end-effector positioning accuracy. Analysis of the time derivative of the dynamic equation and the Lyapunov function show that, when combined with the adaptive law and JA constraint conditions, the quadratic function of the system state error retains a negative semi-definite characteristic [31]. According to Barbalat's lemma, as time approaches infinity, the system state error converges to zero. Under this condition, the control torque boundary is determined by three factors: the upper bound of the spectral norm of the system inertia matrix, the upper bound of the gravity term, and the upper bound of the disturbance observer's compensation torque. These factors ensure the control signal remains bound in the closed-loop system. For parameter adjustment and robustness enhancement, a hierarchical optimization strategy is employed. PID gains are initialized via frequency-domain response analysis, and the hierarchical optimization boundary is set to a step response overshoot of less than 15 % and a rise time of less than 0.1 s. The weight optimization of the adaptive rate matrix is optimized using the PSO algorithm. The objective function is defined as the weighted sum of the absolute error of the integral tracking performance and the energy consumption, and the number of iterations is set to 200. The robust interval of the perturbation observation gain (nominal value ±10 %) is verified by Monte Carlo sampling (sample size $N = 1000$), which evaluates the system stability under parameter perturbation. Sensitivity analysis disturbance conditions−such as ±20 % uncertainty of joint inertia and ±15 % deviation of load mass− are based on variation ranges observed in coal mine operations. The trade-offs in tuning are carefully considered. Increasing proportional gains improves steady-state accuracy, but it also increases the risk of overdraft and oscillation. Improving the adaptive rate can accelerate convergence, but it also raises the computational load. Expanding the robust gain range improves immunity to interference, but it may also reduce nominal performance. The selected technology has proved effective for dealing with multi-objective constraint problems [32]. The method demonstrates robustness by maintaining a trajectory tracking error below 2 % under the following disturbance conditions: uncertainty in joint inertia of ±20 %, deviation in load mass of ±15 %, position error of obstacles of no more than 0.2 meters, and a sudden change in light intensity of no more than 3000 lux. The computational complexity of the research methods mainly stems from the collaborative optimization of multiple controllers, real-time disturbance observer prediction, and dynamic adaptive parameter adjustment. Specifically, the fifth-degree interpolation method reduces the computational complexity of trajectory planning from traditional cubic interpolation $O(n^3)$ to $O(n^2)$ by imposing high-order smoothing constraints on the joint motion trajectory. At the same time, it reduces the number of redundant computing nodes.

In actual coal mining operations, RA uses visual modules and LiDAR to collect real-time spatial information about the roadway. This data is used to identify the obstacle positions and assess lighting conditions, enabling initialization of the DHP model. Smooth joint trajectories are generated using a fifth-degree interpolation method, while the anti-interference tracker dynamically adjusts the interpolation parameters according to the environmental noise. When an obstacle is detected unexpectedly, the adaptive controller triggers local path replanning, constrains joint acceleration, and prevents collisions. The PID controller adjusts the driving torque of each motor joint in a closed-loop manner. Meanwhile, the backstepping adaptive controller adjusts the inertia matrix parameters in real time to accommodate sudden changes in load mass. The disturbance observer, using a composite observation gain, compensates for both weight of the robotic arm and external vibration interference.

3 RESULTS AND DISCUSSION

This section begins by evaluating the performance of the adaptive controller, the fifth-degree interpolation method, and the dynamic function used in the construction of RASM. Next, the actual operational performance of each joint in the simulation model is compared and analyzed. Finally, the RASM is tested under both internal and external disturbance environments, and its performance is compared with other tracking control strategies for comparative analysis of the error control effect.

3.1 Kinematic Modeling Test

The scaled-down test rig is used to simulate the actual working conditions, and the RASM is constructed in MATLAB based on the DHP table. The simulation model is tested to obtain the torque values of each joint of the RA. The simulation model of the RA structural design is verified in real mining environments. After validating both forward and reverse dynamics of the RA, the stability and accuracy of the RA in practical applications are further tested using collected data. Table 1 displays the RA's three-dimensional model derived from the DHPs of the connecting rod CSs.

Table 1. DHP parameter table of RASM

Joint	Joint angle	Z-axis offset [mm]	X-axis offset [mm]	Rotation angle around the X-axis	Range of variation
1	0°	0	1356	0	2000 mm
2	90°	0	3467	45	200 mm
3	0°	148	1732	45	–45°∼45°
4	0°	156	1246	0	3000 mm

The insufficient number of control parameter settings for RA can result in large errors, while excessive loading times in the simulation software slow down model construction. To address these issues, the loading time of the simulation RA model construction is set to 10 s, and the robot displacement step is set to 250. Figure 6 presents the RA simulation structural model, which is based on the Lyapunov function in the adaptive controller. The model illustrates the four workflow processes of telescoping, moving, digging, and carrying. The robotic arm consists of four links with simulated masses of 12.5 kg, 8.2 kg, 6.8 kg, and 4.5 kg, and corresponding lengths of 1356 mm, 3467 mm, 1732 mm, and 1246 mm, respectively. Simulation results indicate that the thrust peaks during telescopic operation are 14,275 N and 13,968 N. The screw torque peaks of mobile operation are 0.1553 Nm and 0.0613 Nm. The screw torque poles of mining operation are 0.9324 Nm and 0.9957 Nm, and the screw torque peaks of handling operation are 0.1677 Nm and 0.1346 N.m. The model illustrate the four workflows. This results confirm that the constructed RASM structure meets the practical requirements of mining operation.

To investigate the effectiveness of the fifth-degree interpolation method used in this study for motion constraint control during RA operations, a comparative analysis is conducted against third-, seventh- and ninth-degrees interpolation methods. Joints 1, 2, and 3 are selected as the test subjects and the fluctuation magnitude of each joint's velocity profile over time is used as the evaluation index. The results are shown in Fig. 7. Application of the interpolation method at different time steps constraints the RA joint motion range, ensuring that the joint curve remains smooth and continuous. Among them, the three times interpolated terminology method shows the weakest constraint performance, with large fluctuations occurring at the start and end of motion. The velocities of Joints 1, 2, and 3 increase from 0 $m \cdot s^{-1}$ to 0.45 $m \cdot s^{-1}$, 0.09 $m \cdot s^{-1}$, and 0.42 $m \cdot s^{-1}$, respectively. The fifth-degree interpolation method demonstrates the best performance, minimizing motion fluctuation in ranges between [−0.2 $m \cdot s^{-1}$, 0.2 $m \cdot s^{-1}$]. Compared with the fifth-degree method, the constraint performance of seven-degree and nine-degree interpolated method improves by 2 % and 3 %, respectively. Furthermore, the fifth-degree interpolation method reduces power consumption and improves the system's energy efficiency ratio while maintaining efficient control. Therefore, the proposed fifth-degree interpolation method offers both high application effectiveness and economic advantage.

To further verify the effect of the interpolation order on RA power consumption, a comparison is made between the third-, fifth- and seventh-degree interpolation methods to verify the superiority of the fifth-degree method. Four different working conditions are used within the same RA application scenario, and the corresponding RA power and time curve are presented in Fig. 8. Among them, Condition 1 is the maximum range of telescopic motion of the robotic arm in an unloaded state; Condition 2 is the extension and contraction motion of the robotic arm under rated load, simulating pushing or supporting operations; Condition 3 simulates the action of drilling or cutting coal and rock using the end effector of the robotic arm; Condition 4 is for the robotic arm to grab and transport materials. Under the four working conditions shown in Fig. 8, the three interpolated term methods exhibit the lowest energy consumption, the seventh-degree method the highest, and the fifth-degree the moderate level. The energy consumption of the three interpolated methods at Condition 1 is 46.37 J, 54.76 J, and 87.45 J, respectively. Compared to the third-degree method, the fifth-degree method improves by 20.32 % while it reduces consumption by 70.23 % compared to seventh-degree method. Across all conditions shown in the figure, all three interpolated methods exhibit the same power consumption results under four different operating conditions, with deviations within 5 %. Although the seventh-degree interpolation method consumes significantly more power than the other two, it does not yield substantial improvement in joint control performance. Therefore, the fifth-degree interpolation method is considered the most reasonable choice, offering a balanced trade-off between control performance and energy efficiency.

To verify the effectiveness of the PID controller perturbed by non-linear environmental factors, the displacement versus time curves of four different joints is analyzed. Moreover, the RA trajectory planning error is combined before and after applying the PID control strategy. The results are shown on Fig. 9. The actual and predicted trajectories of the RA almost completely overlap, with error values not exceeding 5 %. In Fig. 9a, the displacement of Joint 1 reaches 4.2 m with the largest error approximately 0.4 m between actual

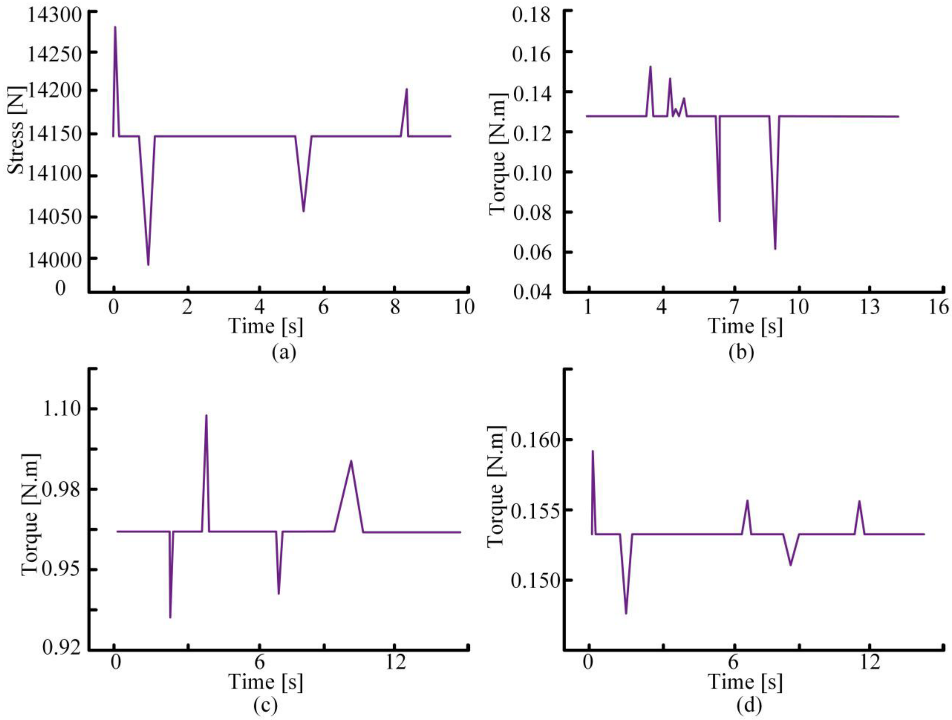

Fig. 6. Dynamic simulation experiment analysis of edge cutting robot; the operational motion process of robot arm simulation structure model in: a) expansion and contract, b) move, c) excavate, and d) carry

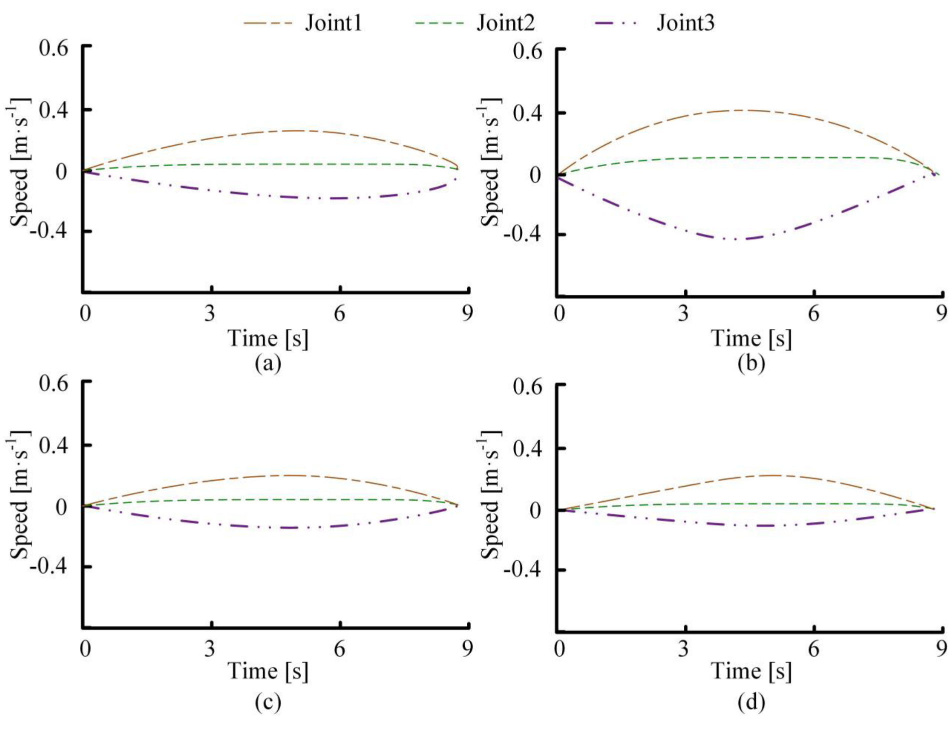

Fig. 7. Comparison of motion speed curves under different interpolation methods: a) fifth degree interpolation method, b) third degree interpolation method, c) seventh degree interpolation method, and d) ninth degree interpolation method

and predicted values. In Figs. 9b and c, Joint 2 exhibits the smallest error, with its actual and predicted displacement curves highly overlapping and differing by less than 0.1 m. Joint 2 and Joint 3 show similar intermediate-level differences, with differences within 1 m. The findings demonstrate the high feasibility of the suggested PID controller in suppressing the environment's unpredictable non-linear variables.

A sensitivity analysis of the key control parameters reveals that increasing the proportional gain from 50 to 70 reduces the steady-state error by 33 % but also raises the overshoot from 4 % to 8 %. Similarly, increasing the adjustment coefficient of the adaptive rate

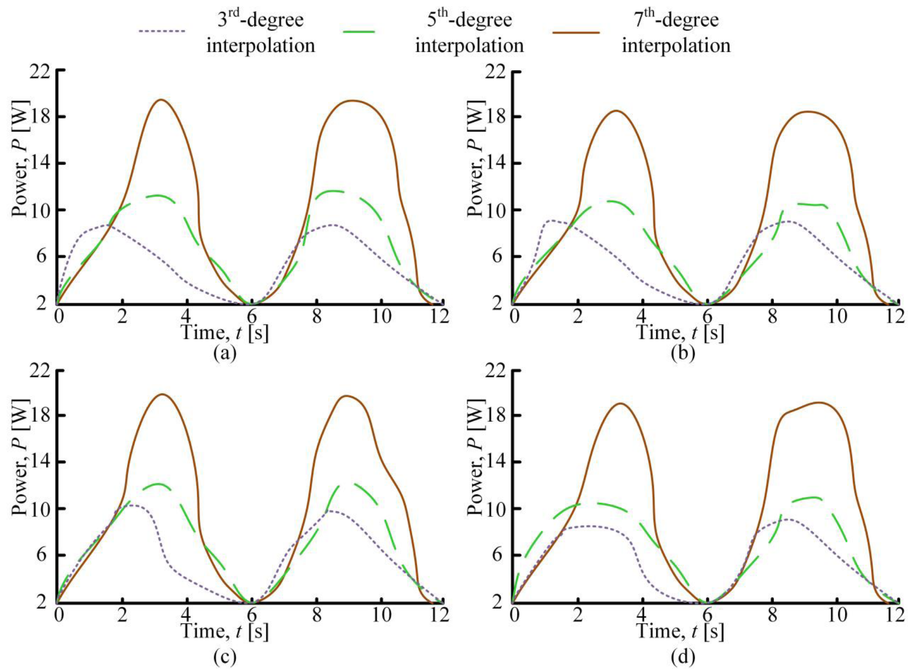

Fig. 8. Power consumption curves of the robot applying the three interpolated term methods at working conditions: a) Condition 1, b) Condition 2, c) Condition 3, and d) Condition 4

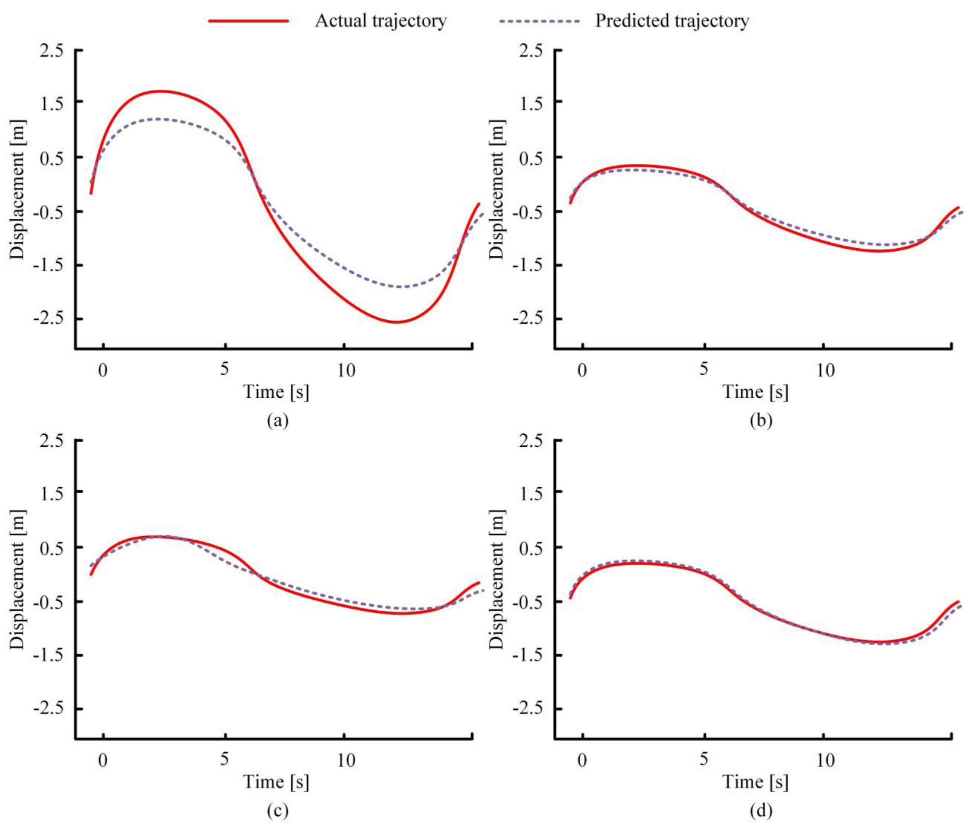

Fig. 9. Performance tests under PID control of RA using: a) displacement curve of joint 1 over time, b) displacement curve of joint 2 over time, c) displacement curve of joint 3 over time, and d) displacement curve of joint 4 over time

matrix increases from 0.5 to 1.0 shortens the convergence time by 22 %, though it increases the computational load by 15 %. Adjusting the disturbance observation gain within ±10 % of the nominal value results in the compensation efficiency of no more than 5 %.

3.2 Practical Application of RASM for Mining Exploitation

After testing the RA model kinematic model, the next step is to verify the motion trajectory error (TE) values of each joint in the simulated robot under externally disturbed conditions. A performance

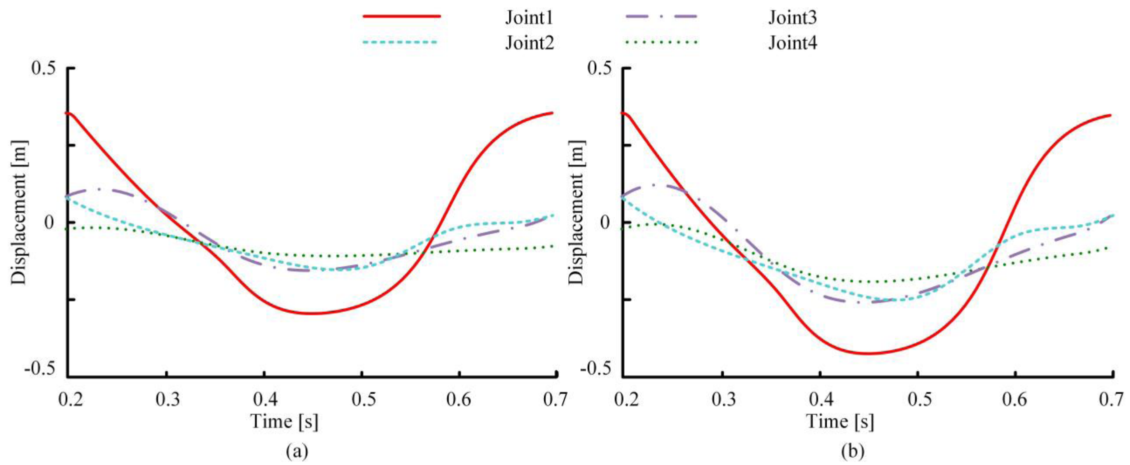

Fig. 10. Comparison of joint error curves under external disturbance conditions; error value of motion trajectory under different environmental conditions a) daytime, and b) nighttime

comparison is conducted between daytime and nighttime environment, and the results are shown in Fig. 10. The fluctuation range of the error value of each joint over time remains in the range of [−0.5 m, 0.5 m]. The largest fluctuation error is observed in Joint 1, reaching an extreme value of −0.4 m at the 0.4-second mark. This is caused by transient motion instability during the initial startup process. The smallest difference occurs in Joint 4, within 0.1 m, due to the adaptive feedback mechanism, which gradually reduces the error. The error values for joints 2 and 3 are medium, ranging from −0.1 to 0.1 m. The RA shows slightly larger errors at night compared to daytime due to reduced camera image acquisition accuracy caused by lower light levels. However, the difference is minimal, within 0.1 m.

To verify the dynamic control effect of the *Simscape* dynamic function applied to the RASM, four rounds of parameter debugging are carried out for each of the four different joints. Comparison and analysis of the positional error over time for each joint during the debugging process is performed, with the results shown in Fig. 11. From the debugging process graphs can be observed that the position errors of the joints gradually converge as the number of debugging times is increased. Among them, the error reduction ratio for Joint 1 is 2 %, 4 %, 3 %, and 1 % when the number of debugging times is 1, 2, 3, and 4, respectively. Moreover, it reaches a stable state in the first 0.2 s, with the best convergence effect. Joint 4 has the slowest convergence only reaching a steady state within 0.4 s. Moreover, its performance is enhanced by an average of 1 % per debugging iteration within the expected range. The debugging performance

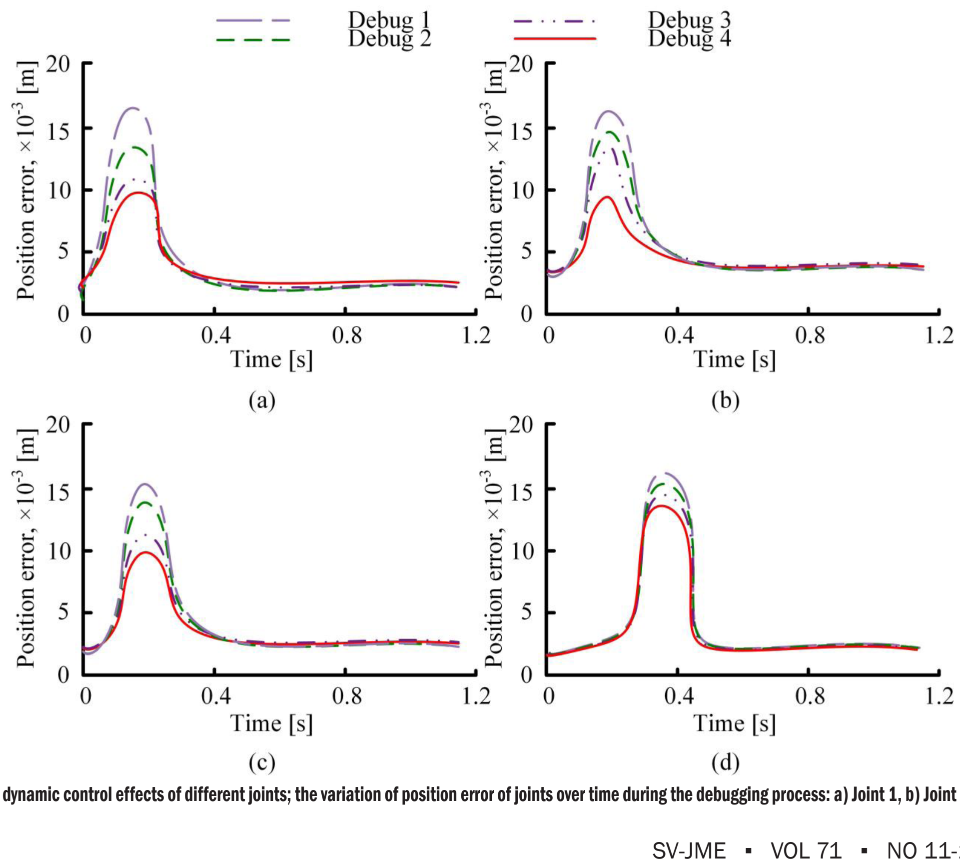

Fig. 11. Comparison of dynamic control effects of different joints; the variation of position error of joints over time during the debugging process: a) Joint 1, b) Joint 2, c) Joint 3, and d) Joint 4

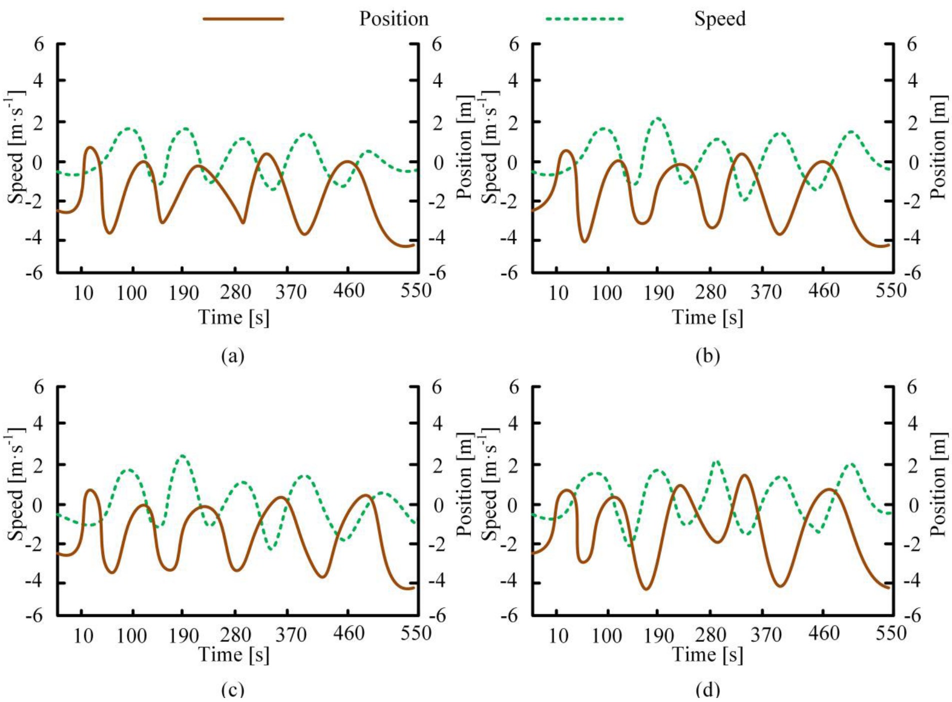

Fig. 12. Comparison of motion continuity under different numbers of obstacles in the paths; Speed and position fluctuation curve of: a) Path 1, b) Path 2, c) Path 3, and d) Path 4

of Joints 2 and 3 shows intermediate performance, stabilizing within 0.3 s and improving performance by an average of 4 % per debugging iteration. All four joints show a performance improvement of over 1 % during each debugging cycle. The results confirm that the proposed *Simscape* dynamic function provides high accuracy and stability for RA error control.

To verify the smoothness of the constructed simulated RA model in terms of joint position and velocity along the obstacle path, four different paths with progressively increasing numbers of obstacles are compared and analyzed. Velocity and position fluctuation curves are used as evaluation indexes, with the results shown in Fig. 12. In Fig. 12a, exhibits the highest stability, with velocity and position fluctuations limited to [$-2\,\text{m·s}^{-1}$, $2\,\text{m·s}^{-1}$] and [$-4\,\text{m·s}^{-1}$, $1\,\text{m·s}^{-1}$], respectively. Path 4 presents largest fluctuation, with maximum displacement of -4.5 at both 180 s and 380 s, respectively. Paths 2 and 3 show intermediate fluctuation level with velocity and position ranges of [$-2.5\ \text{m·s}^{-1}$, $2.5\ \text{m·s}^{-1}$] and [$-4.5\ \text{m·s}^{-1}$, $1.5\ \text{m·s}^{-1}$], respectively. The proposed method allows for the effective planning of trajectories across different paths while keeping velocity and displacement fluctuations within the fixed ranges of [$-4.5\ \text{m·s}^{-1}$, $1.5\ \text{m·s}^{-1}$] and [$-2\ \text{m·s}^{-1}$, $2.5\ \text{m·s}^{-1}$], respectively. The results demonstrate that the adaptive tuning mechanism employed in this study enables the RA to maintain high stability and performance when navigating various obstacle configurations in real mining operations.

To validate the error control performance of the proposed disturbance tracker for the RA, two additional trajectory tracking methods are used for comparison, namely non-linear disturbance observer (NDO) and extended state observer (ESO). The three controllers are applied across four operational processes, namely, excavation, rotation, translation, and handling. The predicted and actual RA trajectory curves for each process are compared and analyzed, with the findings shown in Fig. 13. Predicted and actual trajectories of the RA across all four workflows exhibit a high degree of overlap, with errors below 2 %. In the excavation process (Fig. 13a), the RA shows the largest TE at 0.5 m. In the rotation and translation workflow (Fig. 13b and c), the smallest TE errors are observed at 0.3 m and 0.2 m, respectively. In the handling operation (Fig.13d), the TE is at the level of 0.1 m. The results suggest that the RA applied in a variety of operational processes achieves consistent accuracy with an error below 2 %, with minor fluctuation in individual processes that are operationally negligible.

The performance of EFC proposed is compared before and after parameter reduction and compared with fuzzy controller (FC). The error between the actual and desired displacement is used as the evaluation index, with the results shown on Fig. 14. Under both larger and smaller parameter conditions, the displacement curves of EFC, FC, and the proposed method all show an initial increase followed by a decrease trend, with a total displacement of 0.8 m. Between 7 s and 15 s, the displacement remains constant at around 0.85 m. After parameter reduction, both controllers show hysteresis compared to the desired displacement, although some improvement in motion continuity is observed. For smaller parameters, the proposed method exhibits a hysteresis of 5 % compared to the desired displacement, while FC shows a hysteresis of 10 %. The results show that the proposed controllers have less hysteresis and are more feasible to be used for practical testing.

To further validate the control performance of the proposed method, two comparable methods are selected, namely AC and sliding mode control (SMC). The AC implementation employs Lyapunov stability theory to design adaptive parameter law, with an update rate of 0.5. The SMC implementation uses an exponential approach law with a switching function gain of 150. Experiments are carried out under four typical mining operation processes (tunneling, rotation, translation, and handling), each repeated 10 times. The same DHPs and initial RA state are used, and the same compound disturbances are applied (±20 % sudden change in joint inertia, ±15 % step change in load, 3000 lux pulse disturbing illumination). The performance evaluation is performed using three evaluation indicators: trajectory tracking accuracy, anti-interference ability, and computational complexity. The results are presented in Table 2. The proposed method has a higher computational complexity, but its

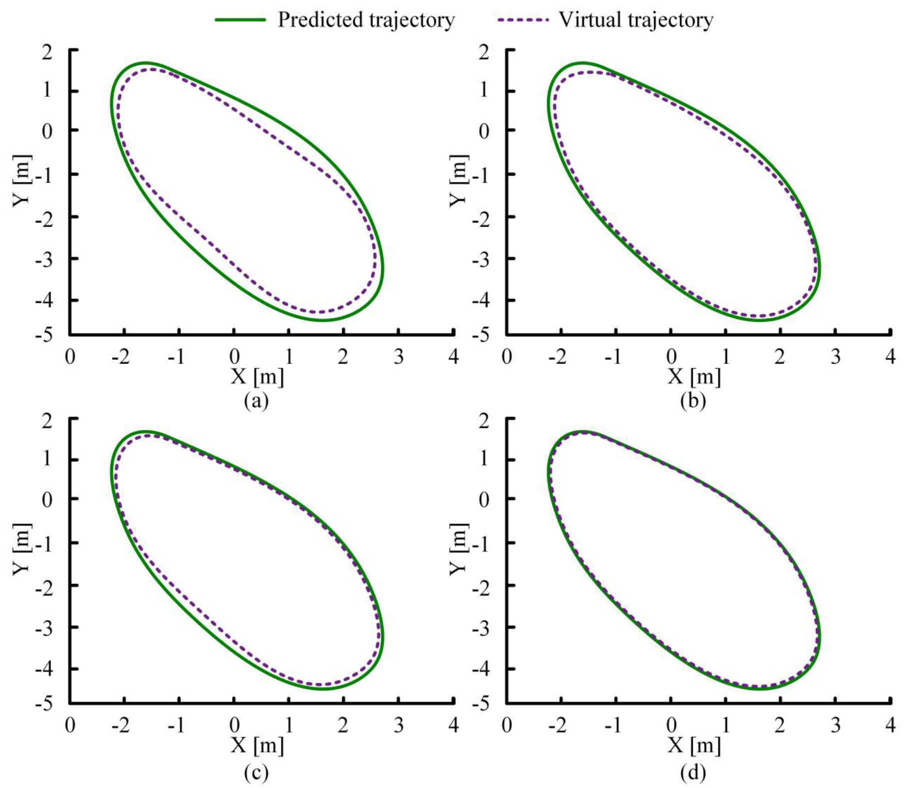

Fig. 13. Error comparison of different trackers; analysis and prediction of trajectory and actual trajectory curve applied to: a) excitation, b) rotation, c) translation, and d) transportation

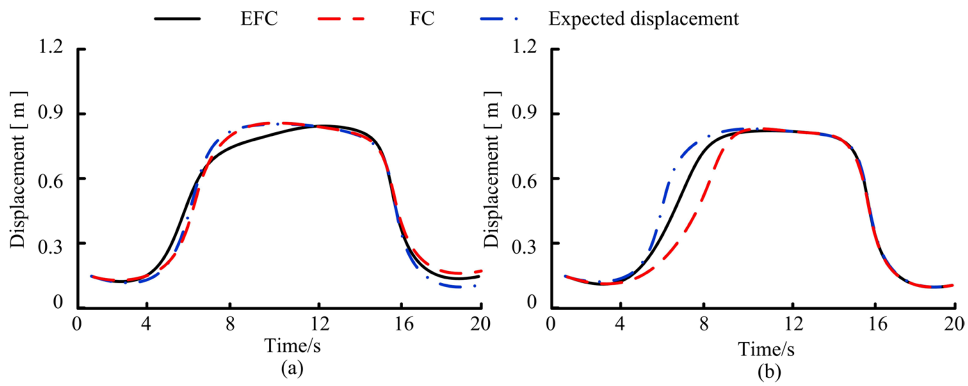

Fig. 14. Comparison of controller parameter size and performance; error between actual displacement and expected displacement under: a) large parameters, and b) smaller parameters

trajectory tracking accuracy is 97 %, which is 10 % and 3 % higher than AC and SMC, respectively. The anti-interference ability is 15 % and 6 % higher than SMC and MEC, respectively. The results indicate that the proposed method can ensure high control accuracy, stability, and reliability in practical control.

To verify the technology's adaptability to the complex environment of a coal mine, simulations were conducted under typical interference conditions, such as fluctuations in dust concentration (50 mg/m^3 to 150 mg/m^3), sudden changes in light intensity (50 lux to 5,000 lux), and mechanical vibrations (5 Hz to 20 Hz). In the simulation, the impact of elevated dust concentration is modeled by accordingly degrading the signal-to-noise ratio (SNR) of the visual feedback module and increasing the joint friction coefficients within the dynamic model. Experimental results show that a peak dust concentration of 150 mg/m^3 causes the end effector's positioning error of 0.18 m. This error increases only by 12 % compared to an ideal environment. When the light intensity is abruptly increased to 5,000 lux, the visual assistance module, using adaptive exposure compensation, maintains the trajectory re-planning delay within 0.2 s. Under continuous vibration interference, the anti-interference tracker reduces the fluctuation amplitude of the joint torque to 28 % of that in the uncontrolled state. These results demonstrate the proposed method can effectively address multi-source, time-varying, and unstructured disturbances in coal mine operations.

Table 2. Performance comparison of various control methods

Control method	Trajectory tracking accuracy [%]	Disturbance rejection capability [%]	Computational complexity (relative value)
AC	87	80	3
SMC	94	89	4
MEC	97	95	2

To verify the superiority of the proposed method, the study further combines it with the advanced model predictive control (MPC), nonlinear active disturbance rejection control (NADRC), and impedance-based method. During the implementation of MPC, a state space model is established. The prediction time domain is five steps, and the control time domain is two steps. For the implementation of the NADRC, the ESO's bandwidth is set to 20 rad/s. For the impedance-based implementation process, the inertia-damping parameter is set to [15, 0.7] N·s/m. The results are shown in Table 3.

As shown in Table 3, the proposed control method's trajectory tracking error of 3 %, which is 5 % higher than the error of MPC and 8 % higher than that of NADRC. Using a composite observer, it predicts and compensates for disturbances caused by sudden changes in simulated dust concentrations and mechanical vibrations, achieving an anti-interference ability of up to 95 %. This performance surpasses NADRC (which depends on nonlinear estimation) and MPC (which depends on model accuracy). Meanwhile, the steady-state time is reduced to 0.24 s through the hierarchical optimization strategy of the proposed control method. The time is 31 % to 40 % shorter than the times of MPC (0.35 s) and NADRC (0.40 s), respectively. It is also suitable for the high real-time requirements of the coal mine environment. Overall, the proposed control method outperforms MPC, NADRC, and impedance-based strategies in terms of trajectory accuracy, anti-interference ability, and energy efficiency. It is particularly suitable for the multi-constrained and complex environment of coal mines.

Table 3. Comparative experiments of advanced methods

Metric	Proposed control method	MPC	NADRC	Impedance-based
Trajectory tracking accuracy [%]	97	92	89	85
Disturbance rejection [%]	95	88	90	80
Settling time [s]	0.24	0.35	0.4	0.5
Energy efficiency [J/cycle]	54.76	68.2	72.5	60.1
Computational complexity (relative value)	4	8	6	3
Robustness parameter range [%]	±20	±15	±10	±25

4 CONCLUSION

Study aimed to develop a kinematics-based tracking control method for operational RAs in coal mining environments. An improved D-H parametric method was utilized to establish the RA linkage CS and workspace, validated through forward/inverse kinematics. A fifth-degree polynomial interpolation was implemented to generate smooth, energy-efficient joint trajectories, thereby minimizing velocity fluctuations. PSO was employed for adaptive rate matrix tuning, while Monte Carlo sampling verified robust perturbation observation gain intervals. The results showed that the proposed method enabled the RA to achieve a thrust limit exceeding 13968 N and the spiral torque limit exceeding 0.0613 Nm under four different operation modes (extension, movement, excavation, and handling). The range of RA motion fluctuation was constrained within [-0.2 m·s^{-1}, 0.2 m·s^{-1}]. To enhance the robustness of the system, it ensured that the velocity and position under different obstacle paths remain within the range of [-2.5 m, 2.5 m] and [-4.5 m, 1.5 m], respectively. These results confirm that the research method can effectively improve the robot's dynamic constraint capabilities against internal and external disturbances. However, certain limitations remain. The control strategy demonstrates limited adaptability to extremely high-frequency mechanical vibrations. Additionally, the vision module's trajectory replanning speed under sudden extreme lighting changes requires optimization. Future research will explore parallel computing architectures to enhance the real-time processing for handling high-frequency disturbances as well as multimodal sensor fusion mechanisms to improve the environmental perception in highly obscured or dynamically changing coal mine environments.

References

[1] Kouritem, S.A., Abouheaf, M.I., Nahas, N., Hassan, M. A multi-objective optimization design of industrial robot arms. *Alex Eng J* 61 12847-12867 (2022) **DOI:10.1016/j.aej.2022.06.052**.

[2] Durairaj, S.P. Quantitative sequential modelling approach to estimate the reliability of computer controlled pneumatically operated pick-and-place robot. *Stroj Vestn-J Mech E* 71 28-35 (2025) **DOI:10.5545/sv-jme.2024.999**.

[3] Richter, F., Lu, J., Orosco, R.K., Yip, M.C. Robotic tool tracking under partially visible kinematic chain: A unified approach. *IEEE Trans Robot* 38 1653-1670 (2021) **DOI:10.1109/tro.2021.3111441**.

[4] Karur, K., Sharma, N., Dharmatti, C., Siegel, J.E. A survey of path planning algorithms for mobile robots. *Vehicles* 3 448-468 (2021) **DOI:10.3390/vehicles3030027**.

[5] Duta, A., Popescu, I., Geonea, I.D., Cretu, S.M., Sass, L., Popa, D.L. Inverse curves-research on two quondam inversor mechanisms. *Stroj Vestn-J Mech E* 69 (2023) **DOI:10.5545/sv-jme.2022.396**.

[6] Lattanzi, L., Cristalli, C., Massa, D.,Boria, S., Lépine, P., Pellicciari, M. Geometrical calibration of a 6-axis robotic arm for high accuracy manufacturing task. *Int J Adv Manuf Technol* 111 1813-1829 (2020) **DOI:10.1007/s00170-020-06179-9**.

[7] Li, Z., Li, S., Francis, A., Luo, X. A novel calibration system for robot arm via an open dataset and a learning perspective. *IEEE T Circuits-II* 69 5169-5173 (2022) **DOI:10.1109/TCSII.2022.3199158**.

[8] Zahaf, A., Bououden, S., Chadli, M., Chemachema, M. Robust fault tolerant optimal predictive control of hybrid actuators with time-varying delay for industrial robot arm. *Asian J Control* 24 1-15 (2022) **DOI:10.1002/asjc.2444**.

[9] Jouila, A., Nouri, K. An adaptive robust nonsingular fast terminal sliding mode controller based on wavelet neural network for a 2-DOF robotic arm. *J Frankl Inst* 357 13259-13282 (2020) **DOI:10.1016/j.jfranklin.2020.04.038**.

[10] Cheng, T., Li, W., Ng, W.Y., Huang, Y., Li, J., Ng, C.S., et al. Deep learning assisted robotic magnetic anchored and guided endoscope for real-time instrument tracking. *IEEE Robot Autom Lett* 6 3979-3986 (2021) **DOI:10.1109/LRA.2021.3066834**.

[11] Lei, M., Feng, K., Ding, S., Wang, M., Dai, Z., Liu, R., et al. Breathable and waterproof electronic skin with three-dimensional architecture for pressure and strain sensing in nonoverlap mode. *ACS Nano* 16 12620-12634 (2022) **DOI:10.1021/acsnano.2c04188**.

[12] Liu, Y., Mei, Y., Cai, H., He, C.,Liu, T., Hu, G.Asymmetric input-output constraint control of a flexible variable-length rotary crane arm. *IEEE Trans Cybern* 52 10582-10591 (2021) **DOI:10.1109/TCYB.2021.3055151**.

[13] Liu, Y, Yao, X, Zhao. W. Distributed neural-based fault-tolerant control of multiple flexible manipulators with input saturations. *Automatica* 156 111202 (2023) **DOI:10.1016/j.automatica.2023.111202**.

[14] Liu, Y., Fu, Y., He, W., Hui, Q. Modeling and observer-based vibration control of a flexible spacecraft with external disturbances. *IEEE Trans Ind Electron* 66 8648-8658 (2018) **DOI:10.1109/TIE.2018.2884172**.

[15] Liu, Y., Guo, F., He, X., Hui, Q. Boundary control for an axially moving system with input restriction based on disturbance observers. *IEEE Trans Syst Man Cybern Syst* 49 2242-2253 (2018) **DOI:10.1109/TSMC.2018.2843523**.

[16] Meng, Q., Lai, X., Yan, Z., Su, C.Y., Wu, M. Motion planning and adaptive neural tracking control of an uncertain two-link rigid-flexible manipulator with vibration amplitude constraint. *IEEE Trans Neural Netw Learn Syst* 33 3814-3828 (2021) **DOI:10.1109/TNNLS.2021.3054611**.

[17] Cui, Z., Li, W., Zhang, X., Chiu, P.W., Li, Z. Accelerated dual neural network controller for visual servoing of flexible endoscopic robot with tracking error, joint motion, and RCM constraints. *IEEE Trans Ind Electron* 69 9246-9257 (2021) **DOI:10.1109/TIE.2021.3114674**.

[18] Piqué, F., Kalidindi, H.T., Fruzzetti, L., Laschi, C., Menciassi, A., Falotico, E. Controlling soft robotic arms using continual learning. *IEEE Robot Autom Lett* 7 5469-5476 (2022) **DOI:10.1109/LRA.2022.3157369**.

[19] Bodie, K., Tognon, M., Siegwart, R. Dynamic end effector tracking with an omnidirectional parallel aerial manipulator. *IEEE Robot Autom Lett* 6 8165-8172 (2021) **DOI:10.1109/LRA.2021.3101864**.

[20] Tong, L., Zhang, M., Ma, H., Wang, C., Peng, L. sEMG-based gesture recognition method for coal mine inspection manipulator using multistream CNN. *IEEE Sens* 23 11082-11090 (2023) **DOI:10.1109/JSEN.2023.3264646**.

[21] Wen, A., Bekris, K. BundleTrack: 6D pose tracking for novel objects without instance or category-level 3D models. *IEEE/RSJ Int Conf Intell Robots Syst* 8067-8074 (2021) **DOI:10.1109/IROS51168.2021.9635991**.

[22] Oliver, G., Lanillos, P., Cheng, G. An empirical study of active inference on a humanoid robot. *IEEE Trans Cogn Dev Syst* 14 462-471 (2021) **DOI:10.1109/TCDS.2021.3049907**.

[23] Qin, J., Du, J. Robust adaptive asymptotic trajectory tracking control for underactuated surface vessels subject to unknown dynamics and input saturation. *J Mar Sci Tech-Japan* 27 307-319 (2022) **DOI:10.1007/s00773-021-00835-9**.

[24] Yan, W., Liu, Y., Lan, Q., Zhang, T., Tu, H. Trajectory planning and low-chattering fixed-time nonsingular terminal sliding mode control for a dual-arm free-floating space robot. *Robotica* 40 625-645 (2022) **DOI:10.1017/S0263574721000734**.

[25] Huang, Y., Li, X., Liu, J., Qiao, Z., Chen, J., Hao, Q. Robotic-arm-assisted flexible large field-of-view optical coherence tomography. *Biomed Opt Express* 12 4596-4609 (2021) **DOI:10.1364/BOE.431318**.

[26] Li, M., Zhu, J., Liu, Q., Liao, H., Zang, K. A novel model predictive current control for fault tolerant permanent magnet vernier rim-driven motor based on improved sector selection. *J Electr Eng Technol* 20 703-712 (2025) **DOI:10.1007/s42835-024-02020-5**.

[27] Scholl, L.Y., Hampp, E.L., de Souza, K.M., Chang, T. C., Deren, M., Yenna, Z.C., et al. How does robotic-arm assisted technology influence total knee arthroplasty implant placement for surgeons in fellowship training? *J Knee Surg* 35 198-203 (2022) **DOI:10.1055/s-0040-1716983**.

[28] Li, L., Li, X., Ouyang, B., Ding, S., Yang, S., Qu, Y. Autonomous multiple instruments tracking for robot-assisted laparoscopic surgery with visual tracking space vector method. *IEEE/ASME Trans Mechatron* 27 733-743 (2021) **DOI:10.1109/TMECH.2021.3070553**.

[29] Wu, J., Liu, Z., Yu, G., Song, Y. A study on tracking error based on mechatronics model of a 5-DOF hybrid spray-painting robot. *J Mech Sci Technol* 36 4761-4773 (2022) **DOI:10.1007/s12206-022-0835-x**.

[30] Lv, N., Liu, J., Jia, Y. Dynamic modeling and control of deformable linear objects for single-arm and dual-arm robot manipulations. *IEEE Int Conf Elect Eng Big Data Algorithm* 38 2341-2353 (2022) **DOI:10.1109/EEBDA53927.2022.9744780**.

[31] Groumpos, P.P. A critical historic overview of artificial intelligence: Issues, challenges, opportunities, and threats. *Artif Intell Appl* 1 197-213 (2023) **DOI:10.47852/bonviewAIA3202689**.

[32] Hebbi, A., Mamatha, H.R. Comprehensive dataset building and recognition of isolated handwritten kannada characters using machine learning models. *Artif Intell Appl* 1 179-190 (2023) **DOI:10.47852/bonviewAIA3202624**

Acknowledgements *The research is supported by: Social contribution of Hunan Science and technology innovation plan, Engineering research and application of automatic knotting equipment for bamboo mat based on biomimetic dexterous hands (No.2020NCK2001).*

Received: 2025-02-26, revised: 2025-06-30, accepted: 2025-07-24 *as Original Scientific Paper.*

Data Availability *All data generated or analyzed during this study are included in this published article.*

Author Contribution *Li Zhou: Conceptualization, Funding acquisition, Investigation, Methodology, Visualization; Writing - original draft, Writing - review & editing; Yan Liu: Data curation, Formal analysis, Supervision, Validation. Writing - original draft, Writing - review & editing. All authors read and approved the final manuscript.*

Kinematična metoda za krmiljenje sledenja za operativno robotsko roko ob upoštevanju kompleksnih zunanjih vplivov

Povzetek *Tveganja, povezana z rudarskimi dejavnostmi v premogovnikih so izjemno visoka, zato je uporaba robotskih rok za nadomeščanje ročnega dela ključnega pomena za izboljšanje varnosti in stroškovne učinkovitosti delovnega procesa. Za obravnavo različnih okoljskih omejitev, kot so prostorske omejitve, ovire ter notranje in zunanje motnje, ta študija predlaga na kinematiki temelječo metodo krmiljenja sledenja in nadzora rudarske robotske roke. Cilj te numerične študije je predlagati metodologijo za ublažitev zunanjih vplivov na stabilnost robotskih rok ter zagotoviti visoko natančnost pri delovanju v zapletenih delovnih pogojih. Rezultati simulacij so pokazali, da predlagana metoda omogoča, da robotska roka dosežе operativne vršne potisne sile, večje od 13.968 N, ter vršne vijačne momente, večje od 0,0613 Nm. Sistem je dosegel stacionarno stanje v povprečju v 0,24 s, pri čemer se je napaka zmanjšala za 2,3 %. V primerjavi z drugimi metodami je sledilnik motenj zmanjšal povprečno napako za 2 %, krmilnik s povratno zanko pa zmanjšal zakasnitev napovedi za 5 %. Predlagana metoda bistveno izboljšuje natančnost in stabilnost pozicioniranja robotskih rok pri rudarskih delih v premogovnikih ter predstavlja obetaven pristop za praktično uporabo.*

Ključne besede *rudarske operacije v premogovnikih, robotska roka, dinamika, kompleksni zunanji vplivi, krmiljenje sledenja*